

Accelerated MR Elastography Using Learned Neural Network Representation

Xi Peng

Affiliations:

Departments of Radiology, Biomedical Engineering, Electronic and Computer Engineering, and Mechanical Engineering, University of Iowa, Iowa City, IA 52246

Running title: MRE Image Reconstruction with Learned Network Representation

Correspondence:

Xi Peng, Ph.D.

Department of Radiology

University of Iowa, Iowa City, IA, 52246

Email: xi-peng@uiowa.edu; stevep1120@gmail.com;

ABSTRACT

Purpose: To develop a deep-learning method for achieving fast high-resolution MR elastography from highly undersampled data without the need of high-quality training dataset.

Methods: We first presented the deep neural network representation as a nonlinear extension of the linear subspace model, then used it to represent and reconstruct MRE image repetitions from undersampled k-space data. The network weights were learned using a multi-level k-space consistent loss in a self-supervised manner. To further enhance reconstruction quality, phase-contrast specific magnitude and phase priors were incorporated, including the similarity of anatomical structures and smoothness of wave-induced harmonic displacement. Experiments were conducted using both 3D gradient-echo spiral and multi-slice spin-echo spiral MRE datasets.

Results: Compared to the conventional linear subspace-based approaches, the nonlinear network representation method was able to produce superior image reconstruction with suppressed noise and artifacts from a single in-plane spiral arm per MRE repetition (e.g., total $R=10$), yielding comparable stiffness estimation to the fully sampled data.

Conclusion: This work demonstrated the feasibility of using deep network representations to model and reconstruct MRE images from highly-undersampled data, a nonlinear extension of the subspace-based approaches.

Keywords: Deep neural network representation; linear subspace; MR Elastography;

1. INTRODUCTION

Brain magnetic resonance elastography (MRE) is a powerful tool to noninvasively access tissue biomechanical properties *in vivo*, with broad potential in various neuroimaging applications including normal pressure hydrocephalus¹, brain tumor², neurodegenerative disease³, cognitive function⁴ and brain development⁵. Higher resolution is particularly important for identifying heterogenous substances and accurately quantifying stiffer tissues. Achieving high-resolution MRE relies on two key factors: fast imaging and robust stiffness inversion. This paper focuses on advancing the fast-imaging component using deep learning-based reconstruction.

MRE is a phase-contrast MRI technique and typically requires the acquisition of multiple imaging repetitions for encoding wave propagation in the 3D vector space (e.g., 6 directions) at varying vibration phase-offsets. As a result, achieving high spatial resolution within a practical scan time is challenging. To address this issue, fast scan such as echo-planer-imaging (EPI) and spiral⁶, along with more efficient motion-encoding strategies have been developed, including SLIM⁷ (sample interval modulation), Ristretto⁸, DENSE^{9, 10} (multiphase Displacement ENcoded Stimulated Echo), Magnetization-Prepared¹¹, and distributed encoding MRE¹². On the other hand, constrained reconstruction from undersampled data has been extensively exploited for fast imaging, with compressed sensing^{13, 14} and low-rank modeling^{15, 16} being among the most widely adopted approaches leveraging the spatial and temporal redundancies. Additionally, anatomical and phase constraints are among the earliest constrained methods used in various MR applications. For instance, the anatomical similarity of a series of MR images has been utilized for denoising and joint image reconstruction via spatially-adaptive regularization^{17, 18}, generalized series model^{19, 20}, group sparsity²¹ and Bayesian modeling²²; Phase regularizations imposing smoothness have been exploited in standard partial Fourier parallel imaging and phase-contrast applications via imaginary component regularization^{23, 24}, structured low-rank approximation²⁵ and direct spatial regularization of the phase with separate magnitude and phase modeling.²⁶⁻²⁸

Recently, deep learning (DL)-based reconstructions have shown considerable promise in producing high quality MR images from under sampled data. However, DL-based reconstruction for MRE is relatively underdeveloped probably because 3D high-resolution high-quality MRE datasets are difficult to acquire for training supervised models²⁹. That said, unsupervised learning-based reconstruction appears to be a natural option for MRE. For example, end-to-end unrolled

networks trained using zero-shot self-supervised learning has been proposed for knee imaging³⁰, cardiac imaging³¹ and quantitative imaging³²; deep image prior (DIP) or manifold representation using a deep neural network have also been successfully developed for cardiac imaging^{33, 34}, quantitative imaging³⁵, upper airway imaging³⁶, and free-breathing pulmonary imaging³⁷.

In this work, we first establish a direct connection between deep neural network representation and linear subspace models, viewing the former as a nonlinear extension of the latter; then we propose to use the neural network representation to reconstruct MRE images from highly undersampled data. Additional elastography-specific priors were further incorporated to improve reconstruction quality. Experiments on both spin-echo and gradient-echo spiral MRE datasets were conducted to demonstrate the feasibility of the proposed method.

2. METHODS

2.1 From Low-rank to Deep Neural Network Representation

According to the partial separability theory¹⁶, a spatiotemporal function $\rho(\mathbf{r}, t) \in \mathbb{C}^{N \times T}$ in MRI can usually be approximated by a linear subspace model, whose matrix form can be expressed as:

$$\rho = UV^H$$

where $U \in \mathbb{C}^{N \times L}$ and $V \in \mathbb{C}^{T \times L}$ are the spatial coefficients and temporal basis, respectively. N is the total number of voxels, T is the total temporal frames/repetitions, L is the model order or the rank. At each time point t , the image function ρ_t can be rewritten as:

$$\rho_t = Uv_t^H$$

where $v_t \in \mathbb{C}^{1 \times L}$ denotes the row vector of V corresponding to time point t . In other words, each image voxel in ρ_t can be considered as a linear combination of elements in v_t with different weights stored in U (i.e., row vectors of U). Moreover, voxels from different time points share the same weights in U . We observed that this linear representation is equivalent to a fully connected layer with identity activation function as illustrated in Fig. 1a. Grounded on this reformulation, the deep network representation can be considered as a nonlinear extension of the linear subspace model by simply replacing the fully connected layer with a deep neural network:

$$\rho_t = G(v_t | \theta)$$

where $G(\cdot)$ is an image generator network or decoder with trainable parameter θ , which creates a feature-based representation of the spatial variations. The temporal variations are also assumed to reside in a low-dimensional manifold represented by the latent vectors, which can be initially derived from measurement data. We note that, implementation-wise, the main distinction between the proposed and existing Time-DIP³³ or manifold learning methods^{34, 36} is that we derive v_t from the linear temporal basis instead of random noise or samples from Gaussian distribution.

2.2 MRE Image Reconstruction with Deep Network Representation

Given $\rho_t = G(v_t|\theta)$, the reconstruction is equivalent to estimating θ and v_t from the measured data. Similar to existing self-supervised approaches^{30, 36}, by substituting the network representation into the forward imaging equation, the cost function for MRE image reconstruction can be written as:

$$\operatorname{argmin}_{\theta, v_t} \sum_{t=1}^T \sum_{i=1}^C \|d_{t,i} - FS_i \rho_t\|_2^2 + \lambda_1 R_{magn}(\rho) + \lambda_2 R_{wave}(\rho) + \lambda_3 R_v(v), \quad (2)$$

where $d_{t,i}$ denotes the k-space data from the t -th repetition and i -th coil. S_i is the coil sensitivity function. Initialized from the temporal basis, the latent vectors $v = \{v_1, v_2, \dots, v_T\}$ contain critical time-dependent information, enabling the nonlinear neural network to generate corresponding temporal images through its powerful and flexible spatial representation capability. To further enhance reconstruction quality, additional regularizations (e.g., R_{magn} and R_{wave}) are introduced to impose anatomical similarity among image repetitions and smoothness of the wave-induced displacement. The network parameters θ and v_t are jointly trained and updated using the above minimization problem in a self-supervised manner. More details are provided below.

2.2.1 Deep network representation with multi-level data consistency

In this work, we used a standard multi-level decoder network to represent the MRE images, combined with multi-level deep supervision³⁸ (i.e., data-consistent losses in our case) that are naturally suited to spiral MRE data (Fig. 2). Specifically, inspired by the Time-DIP³³ method, a three-layer perceptron was first employed to replace the linear fully connected layer in the subspace model, mapping v_t to a feature space with dimension $Q = N/K^2$. K is the total number of levels or scales in the network. Afterwards, a convolutional decoder network was exploited to restore the full resolution image $\rho_{t,K} \in \mathbb{C}^{\sqrt{N} \times \sqrt{N}}$ from the coarsest features $f_{t,1} \in \mathbb{C}^{\sqrt{Q} \times \sqrt{Q}}$. At each

level of the decoder, a linear interpolation operator was used to raise the size of feature maps by a factor of 2, followed by a residual CNN block to learn the higher resolution features.

To better guide the updating of network weights in shallow layers, we adopted the idea of multi-level deep supervision from an early 3D U-net segmentation method³⁸. Specifically, at the end of each level, feature maps $f_{t,k}$ were combined into intermediate images $\rho_{t,k}$ by a single convolutional layer, followed by additional data-consistent losses calculated using corresponding k-space spiral segments $d_{t,i,k}$:

$$\operatorname{argmin}_{\theta, v_t} \sum_{t=1}^T \sum_{i=1}^C \sum_{k=1}^K \|d_{t,i,k} - F_k S_{i,k} \rho_{t,k}\|_2^2 + \lambda_3 R_v(\mathbf{v})$$

where $\rho_{t,k}$ denotes the intermediate image output at the k -th resolution level for repetition t , i.e., $G(v_t | \theta) = \{\rho_{t,1}, \rho_{t,2}, \dots, \rho_{t,K}\}$. F_k and $S_{i,k}$ are the corresponding Fourier transform and coil sensitivity for the k -th resolution. $R_v(\cdot)$ is a regularization imposed on latent vector \mathbf{v} , simply selected to constrain its energy:

$$R_v(\mathbf{v}) = \|\mathbf{v}\|_2^2$$

2.2.2 Magnitude similarity constraint

The magnitude signal capturing the anatomical structures in MRE data remains similar among repetitions. Although a single decoder network is used to model MRE images across different repetitions, the anatomical structures among repetitions might still be able to vary due to the high nonlinearity of the neural network. Therefore, additional constraint is needed to enforce similar anatomical structures among repetitions. Previously, anatomical constraints realized by joint adaptive spatial regularization using reweighted L2 norms have been proposed for reconstruction of diffusion-weighted¹⁸ and MRE³⁹ images respectively. Note that those regularizations were imposed on the complex-valued image quantities. In this work, we propose a different anatomical similarity constraint mainly applied to the magnitude signal at each scale k :

$$R_{magn}(\boldsymbol{\rho}) = \sum_{i,j \in T, i \neq j} \sum_{k=1}^K \|\|\rho_{i,k}| - |\rho_{j,k}|\|_1$$

where $|\cdot|$ takes the magnitude of a complex quantity, $\|\cdot\|_1$ denotes the l_1 norm. Notably, by minimizing the l_1 norm of magnitude differences, magnitude signals are expected to be close but not strictly the same to allow for the potential intravoxel phase disperse⁴⁰. This is also a softer magnitude regularization compared to the separate magnitude and phase models^{26, 28}.

2.2.3 Displacement smoothness

The vibration displacement is encoded in the phase of the MRE images, along with the static image phase. In realistic viscoelastic materials undergoing micron-level harmonic vibrations, such as the brain, tissue displacement can be considered spatially smooth. However, in gradient-echo acquisitions, the static image phase may contain high-frequency components due to tissue susceptibility-induced field variations. Therefore, in this work, we propose to promote only the displacement smoothness of the full resolution image using a standard spatial regularization²⁸:

$$R_{wave}(\boldsymbol{\rho}) = TV(H\boldsymbol{\rho})$$

where $TV(\cdot)$ represents the standard spatial total variation operator. Operation H computes the exponential term of the wave-induced phase components ($\varphi_{dir,p}$), i.e., $H\boldsymbol{\rho} = \{e^{i\varphi_{dir,p}}\}$, for each motion encoding direction and phase offset p . Note that imposing smoothness constraint on the wave-induced phase will not compromise the static anatomical and tissue susceptibility information.

2.3 Implementation Details

The multi-level network was constructed in Pytorch and trained with all MRE repetitions as a single batch (e.g., a batch size of 24 consisting of 4 phase offsets and 6 directions) using stochastic gradient descent with an Adam optimizer on one Nvidia A100 80GB GPU for a fixed number of iterations (500 iterations for the 2D spin-echo dataset and 1000 iterations for the 3D GRE dataset). Complex-valued CNN and activation functions were adopted due to their superior performance in phase-based applications⁴¹. Gaussian noise layers were introduced in the decoder (e.g., in the ResNet) to reduce overfitting during training. To reduce GPU memory cost, training was performed on a “slice-by-slice” basis. For the 3D GRE dataset, Fourier transform and SSC-related phase compensation along the slice direction were first performed³⁹. Each “aliased slice” was then used by our method to unfold the two superimposed slices, similar to the conventional SENSE reconstruction along slice. Because the neural network was used to produce two slices simultaneously in this case, the total number of iterations was doubled in 3D as compared to the 2D case.

The Sigpy package⁴² was adopted to perform non-uniform FFT for spiral image reconstruction. Off-resonance correction was conducted after image reconstruction using a deblurring-based method⁴³. Initial input vectors v_t were computed using singular value decomposition (SVD) from

the center of measured k-space, similar to the subspace-based methods^{15, 16}. The coil-sensitivity and field inhomogeneity maps were obtained separately using a vendor-provided pre-scan. Coil sensitivity maps were then interpolated at different resolution levels for computing the multi-level data consistent loss.

After obtaining the deblurred MRE images, wave-induced displacements were calculated by phase subtraction of the image pairs with positive and negative motion encoding gradient (MEG). Low frequency component (e.g., 3×3) of the displacement field was first removed to reduce bulk motion. Afterwards, a Laplacian based algorithm⁴⁴ was used to unwrap the displacement field, followed by a denoising step using the divergence-free wavelet transformation.⁴⁵ The complex displacement vector fields were then extracted from the 1st harmonic component using temporal Fourier transform. Finally, the displacement fields were further smoothed by a 3D 4th order Butterworth lowpass filter⁴⁶ with a threshold of 100 m⁻¹ before using the algebraic inversion⁴⁷ to produce the complex shear modulus ($G^* = G' + iG''$). Shear stiffness was then computed based on: $\mu_{stiff} = 2|G^*|^2/(G' + |G^*|)$. To quantify the estimated stiffness, the median values were reported within gray matter and white matter respectively, whose masks were segmented from anatomical images using FSL (FMRIB Software Library). The stiffness maps were filtered with a $3 \times 3 \times 3$ median filter for visualization.

2.4 Experiments

In vivo experiments were performed on a 3T MR scanner using a 14-channel receive-only head coil. All experimental data were obtained with the approval of institutional review board and written informed consent was provided from healthy subjects. Mechanical vibrations at 60 Hz were introduced into the subject's head along anterior-posterior using a commercial pneumatic active driver (Resoundant, Rochester, MN) and a cushion-like passive driver placed underneath subjects' head. Four wave-propagation phase offsets were sampled evenly over a single wave period by adjusting the synchronization between the sequence and active driver. Six motion encoding gradients (MEG) along positive and negative x, y, z directions were applied repeatedly to acquire the 3D displacement field. All MRE dataset in this study share the same brain coverage (FOV = 240 \times 240 \times 120 mm³), MEG amplitude and driver vibration strength.

For performance study, a fully sampled multi-slice spin-echo spiral MRE dataset (TR/TE = 3333/50 ms, flip angle = 90°, scan time = 10 minutes, 13.5 ms spiral readout, 5 spiral arms, 2mm

isotropic resolution) and an in-plane fully sampled 3D gradient-echo spiral staircase MRE dataset³⁹ (TR/TE = 66.67/35 ms, FA = 23°, 1.2 × slice oversampling, 2 × through-plane uniform undersampling, scan time = 5 minutes, 13.6 ms spiral readout, 5 spiral arms, 2mm isotropic resolution) were obtained. The spiral arms were then retrospectively downsampled to one arm per repetition interleaving across all repetitions (i.e., each repetition used a different spiral arm), mimicking a total combined in-plane and temporal acceleration factor of 5. (i.e., an acceleration factor of 10 if considering the existing 2× through-plane undersampling of the 3D GRE data, namely only 1 min scan time for 2mm isotropic resolution). Standard SENSE reconstruction, low-rank, and variants of the proposed DL method were conducted and compared.

3. RESULTS

The reconstructed MRE images, displacement and estimated shear stiffness maps (i.e., axial, sagittal and coronal views) from the undersampled 3D GRE and multi-slice SE datasets are shown in Fig. 3 and Fig. 4 respectively, as well as in supplementary Fig. S1 and Fig. S2. As can be seen, conventional SENSE reconstruction suffered from severe aliasing artifacts. The state-of-the-art low-rank reconstruction also exhibited noticeable aliasing artifacts at this acceleration, leading to degraded displacement field and highly underestimated stiffness maps. On the contrary, the network representation method was able to produce high-quality MRE images better delineating anatomical details along with comparable displacement and stiffness estimation. Similar results were observed in both GRE and SE datasets.

To evaluate performance across different acceleration factors, reconstructions were conducted with varying number of undersampled arms and the results are illustrated in Fig. S3. As expected, the low-rank approach was able to produce good-quality MRE images when downsampled to two spiral arms (i.e., out of five fully sampled ones) but significantly compromised when further downsampled to a single spiral arm. This is because the inherent degree of freedom in the MRE dataset with current 24 repetitions is 12 for the linear subspace model¹⁵, namely it only allows a temporal acceleration of less than 2. However, this limit was violated when using only 1 spiral arm across different repetitions. On the other hand, the network representation approach (i.e., without the magnitude similarity and displacement smoothness constraint) consistently generate good-quality MRE images across all acceleration cases, as manifested by the estimated stiffness maps.

Quantitative comparisons of the median stiffness in gray and white matters were reported in Fig. 5. With a single spiral arm, the proposed method produced stiffness measurements comparable to the fully sampled data, while standard SENSE and low-rank methods significantly underestimated shear stiffness due to severe aliasing artifacts and poor SNR (Fig. 5a). Additionally, as the number of spiral arms decreased from 5 to 1, the network method consistently produced reasonable stiffness estimates (i.e., though quantification gradually decreased due to compromise in SNR), while the performance of the lowrank method dropped significantly (Fig. 5b). Lastly, an ablation study was conducted to demonstrate the effectiveness of each component in the proposed method (Fig. S4). Specifically, with the addition of magnitude similarity and displacement smoothness constraints, noise and artifacts were further suppressed.

4. DISCUSSION

Conceptually, we framed the deep neural network representation as a nonlinear extension of the linear subspace model and proposed to use it for MRE image reconstruction from undersampled data. From an implementation perspective, our method differs from exiting manifold learning approaches^{33, 34, 36} in that the latent vectors were initialized using the linear temporal basis rather than random Gaussian noises. Another distinction between our method and previous unrolled self-supervised network methods^{30, 31} is that we used the neural network to represent the spatiotemporal image instead of learning an end-to-end mapping (e.g., unrolled or encoder-decoder architecture) from undersampled data to high-quality images. Thereby, we do not have to separate the already limited data (e.g., 1 spiral arm in our case) into the data consistency layer and loss function respectively. Besides, the network used for image representation is typically much more lightweight than the end-to-end mapping ones.

We demonstrated that the network representation approach could produce high-quality MRE images from a single spiral arm in the in-plane k-space at 2mm resolution while the state-of-the-art low-rank method could not. Additional MRE-specific constraints, including magnitude similarity and displacement smoothness, were further incorporated to suppress noise and artifacts in the magnitude and displacement field. Generally, the proposed method brings the previous 3D GRE spiral staircase acquisition down to 1 minute at 2mm isotropic resolution. Analogous to the spatial coefficients in the linear subspace-based method, the weights of the neural network were estimated purely using the undersampled data.

Although this study primarily used spin-echo and gradient-echo spiral datasets, the approach is adaptable to all sequence types and sampling trajectories. We believe that the proposed method is particularly useful for high-resolution MRE when both higher acceleration and reasonable scan time are desired. Note that, the network representation capability is determined by its own architecture, which may filter out certain desirable or undesirable features in the images. For instance, in the spiral case, the whirling-like artifacts near the nasal cavity due to the effects of T2* accumulated along the spiral readout were less represented by the neural network even when using fully sampled dataset (Fig. S3). The use of more advanced network architecture will be studied in future work. To prevent over fitting, we introduced noise layers in the neural networks and fixed the total number of iterations for 2D and 3D respectively for early stopping. Self-validation scheme could also be adopted.⁴⁸

One limitation of the current study is that conventional algebraic inversion was utilized to derive the stiffness maps which is quite sensitive to noise or any local image artifacts. Therefore, median values were reported for quantitative analysis. Advanced inversion method is the other important pilar for achieving high resolution MRE which is out of the scope of this paper. Another limitation of our method is the relatively long computational time, because it was trained from scratch using a single undersampled dataset. State-of-the-art supervised learning was not fully exploited for MRE due to the lack of ground truth data, but synthesized data might be useful to pretrain the neural networks for MRE image reconstruction. Future work will include incorporating both synthesized data and multiple undersampled data for pretraining and to reduce computational time at inference.

5. CONCLUSION

We presented a self-supervised learning method for improved MRE image reconstruction from highly undersampled data, which can be considered as a nonlinear extension of the linear subspace-based approaches conceptually. We believe this work will serve as an important pilar for advancing high-resolution brain MRE.

REFERENCES

1. Fattahi N, Arani A, Perry A, Meyer F, Manduca A, Glaser K, Senjem ML, Ehman RL, Huston J. MR Elastography Demonstrates Increased Brain Stiffness in Normal Pressure Hydrocephalus. *AJNR Am J Neuroradiol.* 2016;37(3):462-7. Epub 20151105. doi: 10.3174/ajnr.A4560. PubMed PMID: 26542235; PMCID: PMC4792773.
2. Hughes JD, Fattahi N, Van Gompel J, Arani A, Meyer F, Lanzino G, Link MJ, Ehman R, Huston J. Higher-Resolution Magnetic Resonance Elastography in Meningiomas to Determine Intratumoral Consistency. *Neurosurgery.* 2015;77(4):653-8; discussion 8-9. doi: 10.1227/NEU.0000000000000892. PubMed PMID: 26197204; PMCID: PMC4749919.
3. Feng Y, Murphy MC, Hojo E, Li F, Roberts N. Magnetic Resonance Elastography in the Study of Neurodegenerative Diseases. *J Magn Reson Imaging.* 2024;59(1):82-96. Epub 20230421. doi: 10.1002/jmri.28747. PubMed PMID: 37084171.
4. Pavuluri K, Huston J, 3rd, Ehman RL, Manduca A, Jack CR, Jr., Senjem ML, Vemuri P, Murphy MC. Associations between vascular health, brain stiffness and global cognitive function. *Brain Commun.* 2024;6(2):fcae073. Epub 20240229. doi: 10.1093/braincomms/fcae073. PubMed PMID: 38505229; PMCID: PMC10950054.
5. McIlvain G, Schneider JM, Matyi MA, McGarry MD, Qi Z, Spielberg JM, Johnson CL. Mapping brain mechanical property maturation from childhood to adulthood. *Neuroimage.* 2022;263:119590. Epub 20220824. doi: 10.1016/j.neuroimage.2022.119590. PubMed PMID: 36030061; PMCID: PMC9950297.
6. Johnson CL, McGarry MD, Van Houten EE, Weaver JB, Paulsen KD, Sutton BP, Georgiadis JG. Magnetic resonance elastography of the brain using multishot spiral readouts with self-navigated motion correction. *Magn Reson Med.* 2013;70(2):404-12. Epub 20120921. doi: 10.1002/mrm.24473. PubMed PMID: 23001771; PMCID: PMC3529970.
7. Dieter Klatt, Temel K Yasar, Thomas J Royston, Magin RL. Sample interval modulation for the simultaneous acquisition of displacement vector data in magnetic resonance elastography-theory and application. *Phys Med Biol.* 2013;58:8663-75.
8. Guenthner C, Sethi S, Troelstra M, Dokumaci AS, Sinkus R, Kozerke S, Ristretto MRE: A generalized multi-shot GRE-MRE sequence. *NMR Biomed.* 2019;32(5):e4049. Epub 20190129. doi: 10.1002/nbm.4049. PubMed PMID: 30697827; PMCID: PMC6590281.
9. Strasser J, Haindl MT, Stollberger R, Fazekas F, Ropele S. Magnetic resonance elastography of the human brain using a multiphase DENSE acquisition. *Magn Reson Med.* 2019;81(6):3578-87. Epub 20190129. doi: 10.1002/mrm.27672. PubMed PMID: 30693964; PMCID: PMC6590321.
10. Wang R, Chen Y, Yan F, Yang GZ, Feng Y. A 3D fast MR elastography sequence with interleaved multislab acquisition and Hadamard encoding. *Magn Reson Med.* 2025;93(3):1163-75. Epub 20241020. doi: 10.1002/mrm.30342. PubMed PMID: 39428691.

11. Cerjanic AM, Diano AM, Johnson CL. Elastographic magnetization prepared imaging with rapid encoding. *Magn Reson Med.* 2025;93(6):2444-55. Epub 20250311. doi: 10.1002/mrm.30482. PubMed PMID: 40065646; PMCID: PMC12532434.
12. Kramer MK, Cerjanic AM, Johnson CL. Fast, motion-robust MR elastography with distributed, generalized encoding. *Magn Reson Med.* 2025;94(5):2113-28. Epub 20250710. doi: 10.1002/mrm.30631. PubMed PMID: 40638867; PMCID: PMC12283125.
13. Wang R, Chen Y, Li R, Qiu S, Zhang Z, Yan F, Feng Y. Fast magnetic resonance elastography with multiphase radial encoding and harmonic motion sparsity based reconstruction. *Phys Med Biol.* 2022;67(2). Epub 20220125. doi: 10.1088/1361-6560/ac4a42. PubMed PMID: 35016159.
14. Lustig M, Donoho D, Pauly JM. Sparse MRI: The application of compressed sensing for rapid MR imaging. *Magn Reson Med.* 2007;58(6):1182-95. doi: 10.1002/mrm.21391. PubMed PMID: 17969013.
15. McIlvain G, Cerjanic AM, Christodoulou AG, McGarry MDJ, Johnson CL. OSCILLATE: A low-rank approach for accelerated magnetic resonance elastography. *Magn Reson Med.* 2022;88(4):1659-72. Epub 20220601. doi: 10.1002/mrm.29308. PubMed PMID: 35649188; PMCID: PMC9339522.
16. Liang Z-P. SPATIOTEMPORAL IMAGING WITH PARTIALLY SEPARABLE FUNCTIONS. 2007 4th IEEE International Symposium on Biomedical Imaging: From Nano to Macro. 2007:988-91. doi: 10.1109/ISBI.2007.357020.
17. Haldar JP, Hernando D, Song SK, Liang ZP. Anatomically constrained reconstruction from noisy data. *Magn Reson Med.* 2008;59(4):810-8. doi: 10.1002/mrm.21536. PubMed PMID: 18383297.
18. Haldar JP, Wedeen VJ, Nezamzadeh M, Dai G, Weiner MW, Schuff N, Liang ZP. Improved diffusion imaging through SNR-enhancing joint reconstruction. *Magn Reson Med.* 2013;69(1):277-89. Epub 20120305. doi: 10.1002/mrm.24229. PubMed PMID: 22392528; PMCID: PMC3407310.
19. Liang ZP, Lauterbur PC. A generalized series approach to MR spectroscopic imaging. *IEEE Trans Med Imaging.* 1991;10:132-7.
20. Peng X, Ying L, Liu Q, Zhu Y, Liu Y, Qu X, Liu X, Zheng H, Liang D. Incorporating reference in parallel imaging and compressed sensing. *Magn Reson Med.* 2015;73(4):1490-504. Epub 20140425. doi: 10.1002/mrm.25272. PubMed PMID: 24771404.
21. Trzasko J, Manduca A. Group Sparse Reconstruction of Vector-Valued Images. *Proc Intl Soc Mag Reson Med* 19. 2011:2839.
22. Bilgic B, Goyal VK, Adalsteinsson E. Multi-contrast reconstruction with Bayesian compressed sensing. *Magn Reson Med.* 2011;66(6):1601-15. Epub 20110610. doi: 10.1002/mrm.22956. PubMed PMID: 21671267; PMCID: PMC3175273.
23. Bydder M, Robson MD. Partial fourier partially parallel imaging. *Magn Reson Med.* 2005;53(6):1393-401. doi: 10.1002/mrm.20492. PubMed PMID: 15906299.

24. Kim TH, Setsompop K, Haldar JP. LORAKS makes better SENSE: Phase-constrained partial fourier SENSE reconstruction without phase calibration. *Magn Reson Med.* 2017;77(3):1021-35. Epub 20160401. doi: 10.1002/mrm.26182. PubMed PMID: 27037836; PMCID: PMC5045741.
25. Haldar JP. Low-rank modeling of local k-space neighborhoods (LORAKS) for constrained MRI. *IEEE Trans Med Imaging.* 2014;33(3):668-81. doi: 10.1109/TMI.2013.2293974. PubMed PMID: 24595341; PMCID: PMC4122573.
26. Mohammed S, Kozlowski P, Salcudean S. Phase-regularized and displacement-regularized compressed sensing for fast magnetic resonance elastography. *NMR Biomed.* 2023;36(7):e4899. Epub 20230201. doi: 10.1002/nbm.4899. PubMed PMID: 36628624.
27. Ong F, Cheng JY, Lustig M. General phase regularized reconstruction using phase cycling. *Magn Reson Med.* 2018;80(1):112-25. Epub 20171121. doi: 10.1002/mrm.27011. PubMed PMID: 29159989; PMCID: PMC5876131.
28. Zhao F, Noll DC, Nielsen JF, Fessler JA. Separate magnitude and phase regularization via compressed sensing. *IEEE Trans Med Imaging.* 2012;31(9):1713-23. Epub 20120426. doi: 10.1109/TMI.2012.2196707. PubMed PMID: 22552571; PMCID: PMC3545284.
29. Shan X, Yang J, Xu P, Hu L, Ge H. Deep neural networks for magnetic resonance elastography acceleration in thermal-ablation monitoring. *Med Phys.* 2022;49(3):1803-13. Epub 20220204. doi: 10.1002/mp.15471. PubMed PMID: 35061250.
30. Yaman B, Hosseini SAH, Moeller S, Ellermann J, Ugurbil K, Akcakaya M. Self-supervised learning of physics-guided reconstruction neural networks without fully sampled reference data. *Magn Reson Med.* 2020;84(6):3172-91. Epub 20200702. doi: 10.1002/mrm.28378. PubMed PMID: 32614100; PMCID: PMC7811359.
31. Yaman B, Shenoy C, Deng Z, Moeller S, El-Rewaidy H, Nezafat R, Akcakaya M. Self-Supervised Physics-Guided Deep Learning Reconstruction for High-Resolution 3D LGE CMR. 2021 IEEE 18th International Symposium on Biomedical Imaging (ISBI)2021. p. 100-4.
32. Bian W, Jang A, Liu F. Improving quantitative MRI using self-supervised deep learning with model reinforcement: Demonstration for rapid T1 mapping. *Magn Reson Med.* 2024;92(1):98-111. Epub 20240211. doi: 10.1002/mrm.30045. PubMed PMID: 38342980; PMCID: PMC11055673.
33. Yoo J, Jin KH, Gupta H, Yerly J, Stuber M, Unser M. Time-Dependent Deep Image Prior for Dynamic MRI. *IEEE Trans Med Imaging.* 2021;40(12):3337-48. Epub 20211130. doi: 10.1109/TMI.2021.3084288. PubMed PMID: 34043506.
34. Zou Q, Ahmed AH, Nagpal P, Kruger S, Jacob M. Dynamic Imaging Using a Deep Generative SToRM (Gen-SToRM) Model. *IEEE Trans Med Imaging.* 2021;40(11):3102-12. Epub 20211027. doi: 10.1109/TMI.2021.3065948. PubMed PMID: 33720831; PMCID: PMC8590205.
35. Slavkova KP, DiCarlo JC, Wadhwa V, Kumar S, Wu C, Virostko J, Yankeelov TE, Tamir JI. An untrained deep learning method for reconstructing dynamic MR images from accelerated model-based data. *Magn Reson Med.* 2023;89(4):1617-33. Epub 20221205. doi: 10.1002/mrm.29547. PubMed PMID: 36468624; PMCID: PMC9892348.

36. Rushdi Zahid Rusho, Qing Zou, Wahidul Alam, Subin Erattakulangara, Mathews Jacob, Lingala SG. Accelerated Pseudo 3D Dynamic Speech MR Imaging at 3T Using Unsupervised Deep Variational Manifold Learning. Medical Image Computing and Computer Assisted Intervention – MICCAI2022.
37. Qing Zou, Luis A. Torres, Sean B. Fain, Nara S. Higano, Alister J. Bates, Jacob M. Dynamic imaging using motion-compensated smoothness regularization on manifolds (MoCoSToRM). *Phys Med Biol.* 2022;67.
38. Zeng G, Yang X, Li J, Yu L, Heng P-A, Zheng G. 3D U-net with Multi-level Deep Supervision: Fully Automatic Segmentation of Proximal Femur in 3D MR Images. *Machine Learning in Medical Imaging: Springer International Publishing*; 2017. p. 274–82.
39. Peng X, Sui Y, Trzasko JD, Glaser KJ, Huston J, 3rd, Ehman RL, Pipe JG. Fast 3D MR elastography of the whole brain using spiral staircase: Data acquisition, image reconstruction, and joint deblurring. *Magn Reson Med.* 2021;86(4):2011-24. Epub 20210607. doi: 10.1002/mrm.28855. PubMed PMID: 34096097; PMCID: PMC8498799.
40. Glaser KJ, Felmlee JP, Manduca A, Ehman RL. Shear stiffness estimation using intravoxel phase dispersion in magnetic resonance elastography. *Magn Reson Med.* 2003;50(6):1256-65. doi: 10.1002/mrm.10641. PubMed PMID: 14648574.
41. Cole E, Cheng J, Pauly J, Vasanawala S. Analysis of deep complex-valued convolutional neural networks for MRI reconstruction and phase-focused applications. *Magn Reson Med.* 2021;86(2):1093-109. Epub 20210316. doi: 10.1002/mrm.28733. PubMed PMID: 33724507; PMCID: PMC8291740.
42. Ong F, Lustig M. SigPy: A Python Package for High Performance Iterative Reconstruction. In *Proc Intl Soc Mag Reson Med.* 2019:4819.
43. Wang D, Zwart NR, Pipe JG. Joint water-fat separation and deblurring for spiral imaging. *Magn Reson Med.* 2018;79(6):3218-28. Epub 20171005. doi: 10.1002/mrm.26950. PubMed PMID: 28983966.
44. Schofield MA, Zhu Y. Fast phase unwrapping algorithm for interferometric applications. *Optics Letters.* 2003;28(14):1194-6. doi: doi.org/10.1364/OL.28.001194.
45. Ong F, Uecker M, Tariq U, Hsiao A, Alley MT, Vasanawala SS, Lustig M. Robust 4D flow denoising using divergence-free wavelet transform. *Magn Reson Med.* 2015;73(2):828-42. Epub 20140218. doi: 10.1002/mrm.25176. PubMed PMID: 24549830; PMCID: PMC4139475.
46. Streitberger KJ, Reiss-Zimmermann M, Freimann FB, Bayerl S, Guo J, Arlt F, Wuerfel J, Braun J, Hoffmann KT, Sack I. High-resolution mechanical imaging of glioblastoma by multifrequency magnetic resonance elastography. *PLoS One.* 2014;9(10):e110588. Epub 20141022. doi: 10.1371/journal.pone.0110588. PubMed PMID: 25338072; PMCID: PMC4206430.
47. Oliphant TE, Manduca A, Ehman RL, Greenleaf JF. Complex-Valued stiffness reconstruction for magnetic resonance elastography by algebraic inversion of the differential equation. *Magnetic Resonance in Medicine.* 2001;45:299–310.

48. Rusho RZ, Ahmed AH, Kruger S, Alam W, Meyer D, Howard D, Story B, Jacob M, Lingala SG. Prospectively accelerated dynamic speech magnetic resonance imaging at 3 T using a self-navigated spiral-based manifold regularized scheme. *NMR Biomed.* 2024;37(8):e5135. Epub 20240305. doi: 10.1002/nbm.5135. PubMed PMID: 38440911.

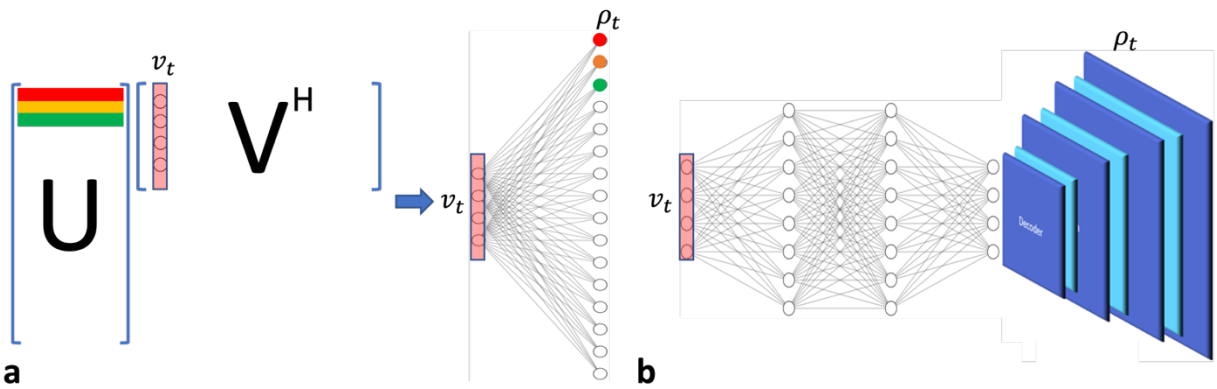


Figure 1. Illustration of a) the linear subspace model and b) the deep neural network representation as the nonlinear extension.

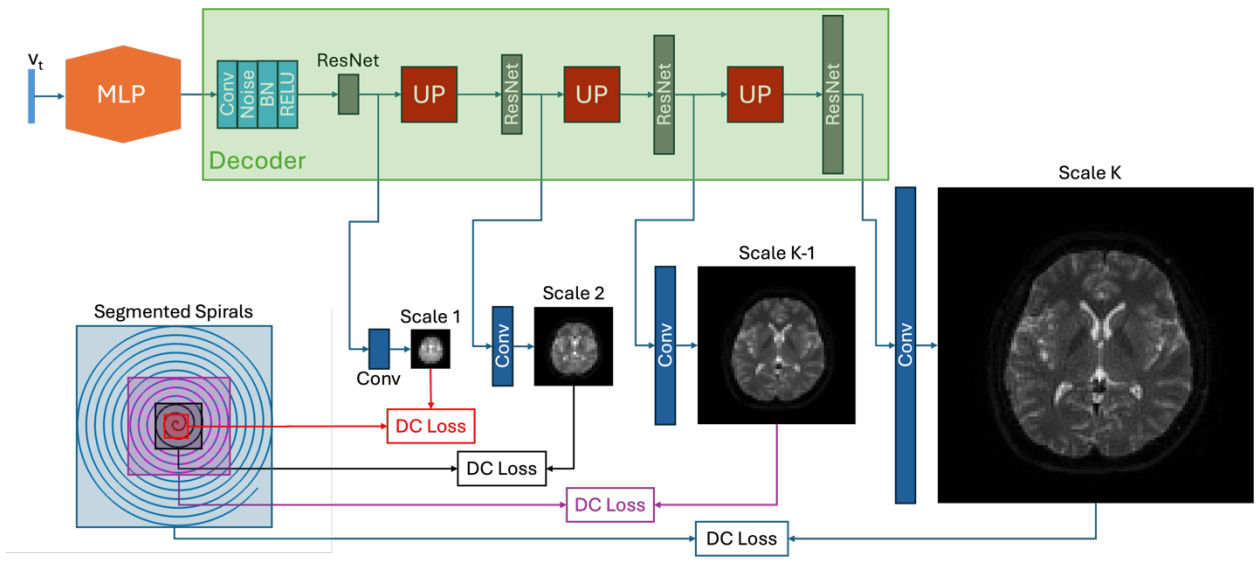


Figure 2. The multi-level architecture of the neural network decoder with multi-level k-space consistent losses.

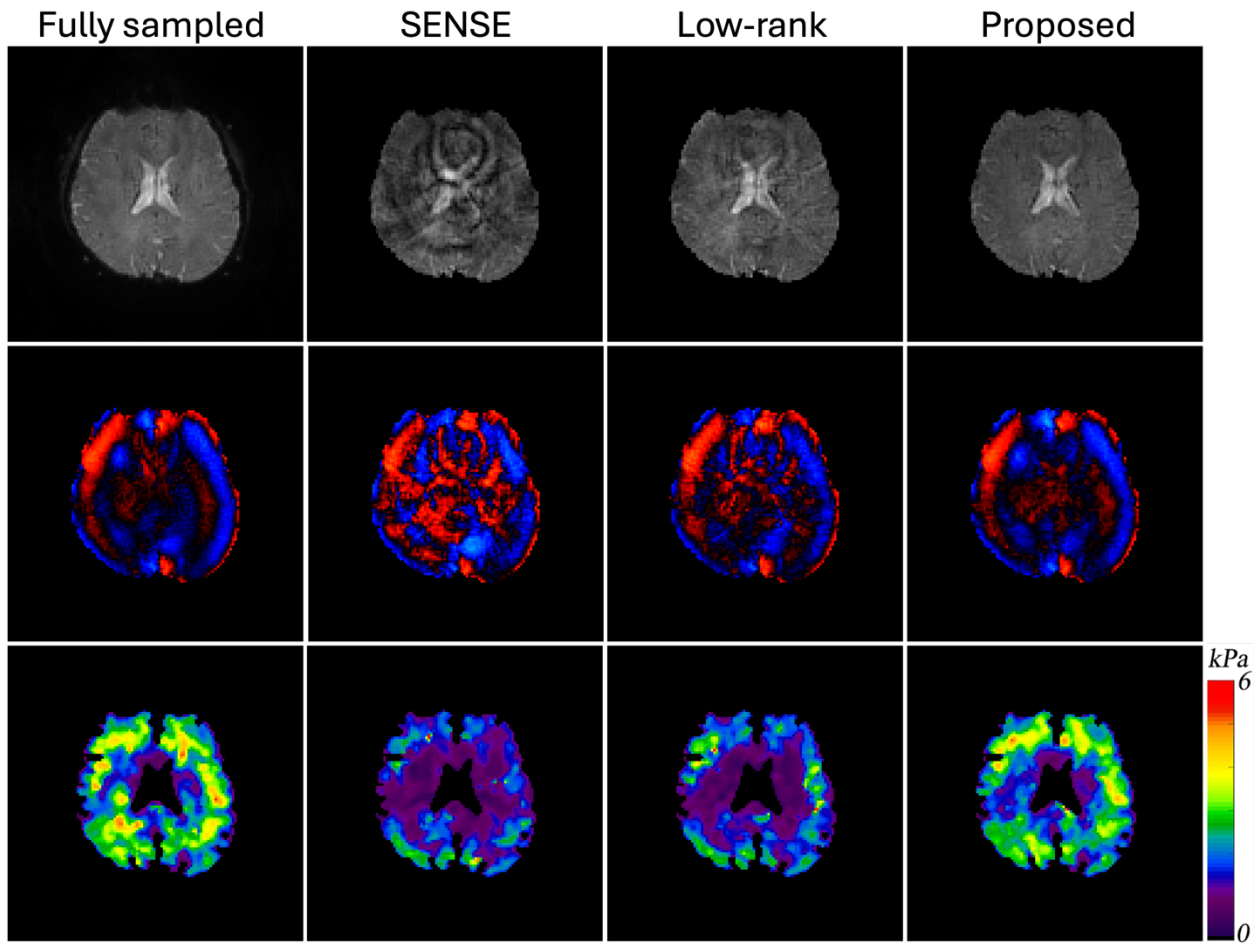


Figure 3. Reconstructed MRE images, displacement (along y direction) and stiffness maps using a single spiral arm (out of the fully sampled 5 spirals) from the 3D GRE-SSC dataset (i.e., a total reduction factor of 10 if accounting for the $2\times$ through-plane acceleration).

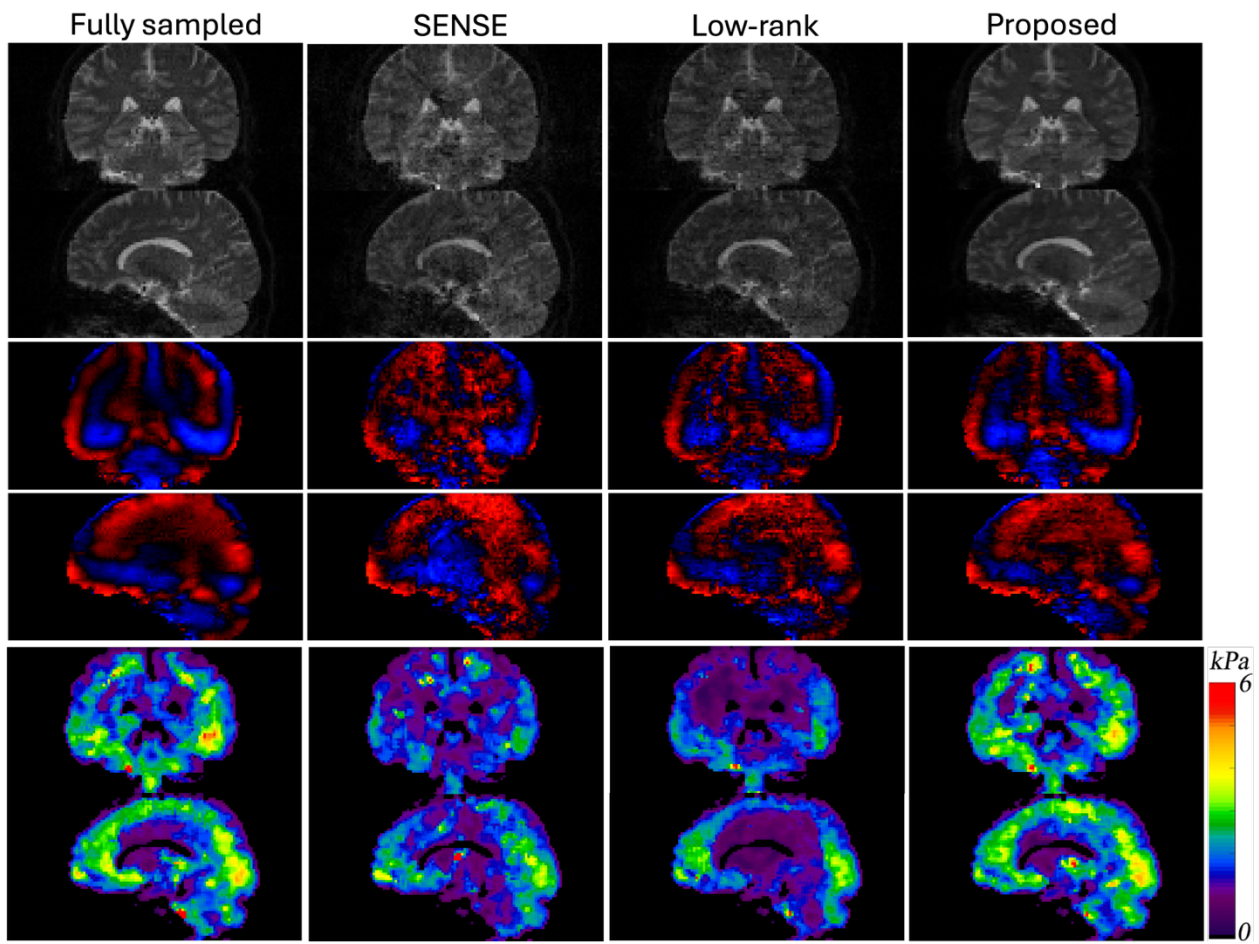


Figure 4. Reconstructed MRE images, displacement (along y direction) and stiffness maps using only 1 spiral arm (out of fully sampled 5 spirals) from the multi-slice spin-echo dataset.

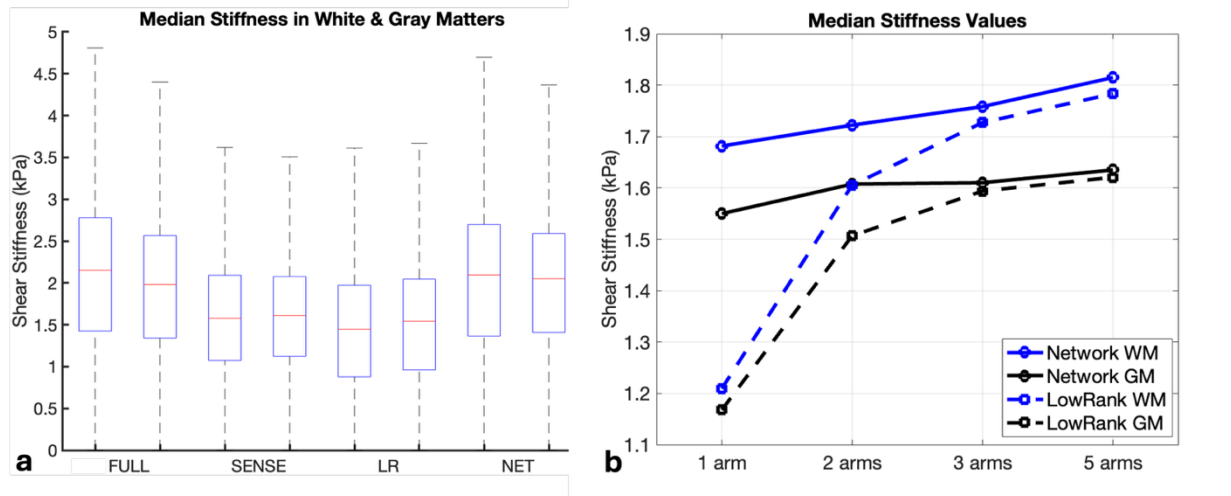


Figure 5. Quantitative comparison of median stiffness in white and gray matters across different methods and undersampling factors. a) Stiffness estimated from the spin-echo dataset using SENSE, low-rank and the proposed DL methods from a single spiral arm (left bar: white matter; right bar: gray matter). b) Stiffness estimated from the 3D gradient-echo dataset using the low-rank and the proposed DL methods with varying number of spiral arms.